Analysis and Experimental Implementation of Grid Frequency Regulation Using Behind-the-Meter Batteries Compensating for Fast Load Demand Variations

Young-Jin Kim, *Member, IEEE*, Gerard Del-Rosario-Calaf, and Leslie K. Norford

Abstract—This paper proposes a new grid frequency regulation (GFR) scheme using behind-the-meter battery energy storage systems (BESSs). The fast dynamic responses of the electrical BESSs enable buildings to compensate for the high-frequency components of load demand variations, through direct load control (DLC). An electrical system in a building, along with its building-level and device-level controllers, is considered to address the difficulties in the application of DLC, especially in communicating with several small-scale BESSs. A small-signal analysis is carried out using the aggregated responses of the generators and the DLC-enabled buildings to investigate the proposed GFR scheme, particularly with respect to the feedback controllers for the buildings. Simulation studies are performed using a test grid for various penetrations of the DLC-enabled buildings, and the test grid is implemented using a laboratory-scale microgrid. The proposed GFR is effective in reducing the frequency deviations and required reserve capacity of the generators, which is achieved by making small variations in the state-of-charge of the behind-the-meter battery.

Index Terms—Behind-the-meter battery energy storage systems (BESSs), direct load control (DLC), grid frequency regulation (GFR), laboratory-scale microgrid.

NOMENCLATURE

The main notation used in this paper is summarized here. The subscripts b or B represent individual or aggregated building BESSs, respectively. Similarly, the subscripts g or G represent individual or aggregated generators, respectively.

A. Acronyms:

BESS	Battery energy storage system.
BPC	Building power controller.
DLC	Direct load control.
DG	Distributed generator.
DR	Demand response.
FRR	Frequency regulation reserve.
GFR	Grid frequency regulation.
ISO	Independent system operator.
LC-PID	PID combined with a lead compensator.
LPF (HPF)	Low (high) pass filter.
MPPT	Maximum power point tracking.
PCL	Programmable current limiter.
PEV	Plug-in electric vehicle.
PFC	Primary frequency control.
PPD	PEV power distributor.
SFC	Secondary frequency control.
SOC	State-of-charge.
V2G	Vehicle-to-grid.
VC-CV	Variable-current constant-voltage.
ZIP	Impedance, current, and power.

B. Set:

peak, rated, ref, max, DC	Subscript for peak, rated, reference, maximum, and building DC-link values.
Δf	Grid frequency deviation in t/s-domains.

C. DLC-Enabled Building and DLC Signal Distribution:

K, L	Total number of PEVs and number of PEVs available for GFR.
k, h, u	Index of K, L, and $(K\text{-}L)$ PEVs in a building.
$D_{\text{inv\_ref}}, D_{\text{pv\_ref}}, D_{\text{ev\_ref}}, D_{\text{load\_ref}}$	Reference duty ratios of an AC-DC inverter, a PV generator, PEVs, and building loads.
$V_{\text{DC}}, P_{\text{inv}}$	DC-link voltage and output power of an AC-DC inverter.
$V_{\text{pv}}, P_{\text{pv}}$	Output voltage and power of a PV generator.
$V_{\text{load}}, P_{\text{load}}$	Input voltage and power of DC loads.
PEV_k	k^{th} PEV.
$V_{\text{ev}}^k, S_{\text{ev}}^k, t_d^k$	Input voltage, SOC level, and scheduled charging time period of PEV_k.
$P_{\text{ev}}^k, P_{\text{ev\_ss}}^k$	Instantaneous and steady-state input power of PEV_k (i.e., $P_{\text{ev}}^k = P_{\text{ev\_ss}}^k + \Delta P_{\text{ev}}^k$).
r_k	Ratio of the input power of PEV_k to total PEV input power.
$P_{\text{tot\_ev}}$	Total input power of PEVs in a building.
P_b	Total building input power (i.e., $P_b = P_{\text{tot\_ev}} + P_{\text{load}} - P_{\text{pv}}$).

ΔP_{b_ref}	Incremental input power reference of a building, equivalent to a DLC signal.
P_sur	Surplus power inside a building.
R_b	Droop constant for PFC of a building.

D. Small-Signal Analysis:

M, D	Moment of generators' inertia and load-damping constant.
T_G, T_T, T_B, T_F	Time constants of governors, turbines, building BESSs, and an LPF.
R_G, R_B	Droop constants for generators and BESSs.
Δf_G, Δf_B	Low/high-frequency components of Δf.
ΔP_G, ΔP_B, ΔP_L	Incremental power of generators, BESSs, and loads.
ΔP_{G_ref}, ΔP_{B_ref}	Incremental power reference of generators and BESSs
$B(s)$	Secondary frequency controller of BESSs.
PI_G, P_g, I_g	PI controller and its gains for SFC of generators.
P_b, I_b, D_b	PID controller gains in $B(s)$.
N_1	Parameter of a limiter for a D controller.
N_{2-4}	Parameters of a phase-lead compensator.
s_{0-6}	Boundaries of target frequency ranges.
t_max	Maximum communication time delays.

E. Simulation and Experimental Case Studies:

P_G, P_B, P_L, P_PV	Instantaneous power of generators, BESSs, loads, and PV systems.
$P_{\text{Gs\_ref}}$, P_{Bs_ref}	Reference signals for SFC of generators and BESSs.
P_{b_max}	Maximum building input power.
NG, NB	Numbers of generators and building BESSs.
$\alpha_{1-\text{NG}}$, $\beta_{1-\text{NB}}$	Participation factors for SFC of generators and groups of DLC-enabled buildings.
t_dg, t_db	2-second time delay in SFC.
f_Hg, f_Lg, f_Hb, f_Lb	High/low dead-band limits of Δf_G and Δf_B.
t_sampling	Sampling time of Δf.
r, x	Transformer resistance and reactance.
$\Delta f_\text{peak-to-peak}$, Δf_rms	Peak-to-peak and root-mean-square Δf.
avg. dΔP_G/dt, max. dΔP_G/dt	Average and maximum values of absolute ramp-rates of P_G.
std. ΔP_B	Standard deviation of BESS input power.
ΔSOC	SOC variation of the Li-ion battery pack.
t_C, t_L, t_H	Instances to receive and transmit signals of central/local controllers and hardware units.

I. INTRODUCTION

THE number and duration of grid frequency deviations have become non-negligible, even in large-scale power grids such as U.S. Interconnections [1]. These frequency deviations can cause not only malfunction of the end-use devices but also frequency instability in the entire network. The frequency deviations may be more severe in smaller isolated grids, in which the moment of inertia of the generator units, and load damping, are not sufficiently large. Generators have to respond excessively to commands from an independent system operator (ISO) to compensate for this increased imbalance; thereby incurring higher operational stress and requiring a larger frequency regulation reserve (FRR) capacity. Therefore, current frequency control practices, responsible for maintaining a nominal grid frequency, need to be clearly understood and re-considered to improve frequency stability [1].

Several residential and commercial buildings that recently included behind-the-meter electrical energy storage systems have received considerable attention from ISOs owing to their usefulness in applications related to demand response (DR) [2]. For example, Stem Inc. has introduced wall-mounted battery energy storage systems (BESSs) for building owners to manage the building peak demand, reducing electricity costs [3]. Behind-the-meter BESSs also increase the maximum capacity of rooftop photovoltaic (PV) generators by preventing intermittent output power from being supplied directly to electrical networks, especially when the building load becomes low. In addition, commercial buildings have been equipped with multiple charging stations for plug-in electric vehicles (PEVs). The PEVs are expected to be connected to the electricity grid, through the building power lines, for most of the day [4], and can be used for building energy storage. Using behind-the-meter electrical batteries, the buildings can provide ancillary services to reduce frequency deviations and mitigate the FRR requirements imposed on generator units [5].

Electric batteries have high energy densities and rapid dynamic responses, which make them suitable for high- frequency and high-power cyclic operations. Reduction of battery life is caused mainly by the deep discharge encountered while driving, rather than by small swings in the state-of-charge (SOC) resulting from direct load control (DLC) [6]. Direct control of PEV batteries for grid frequency regulation (GFR) has been widely studied, with and without considering PEV mobility behavior [5], [7]–[17]; e.g., the response of PEVs to primary frequency control (PFC) signals was investigated in [7]–[11]. A proportional controller, followed by a dead-band function, was used to adjust the PEV input power [7]. In [8], a high-pass filter was used for the PFC of PEVs, which reduced the battery power capacity required for a stabilized GFR. A participation factor of DLC-enabled PEVs was determined using statistical data, to reflect their aggregated dynamic response in PFC [9]. In [10], PEVs responded to PFC signals mainly via vehicle-to-grid (V2G) methods. V2G control was further investigated for GFR ancillary service provision and cost-effective battery energy management [11]. However, these papers considered only

the supplementary PFC. In [12] and [13], the V2G control was applied to support secondary frequency control (SFC), considering the battery charging demand. The charging-rate control of PEVs was studied to combine SFC with PEV agent policies [14]. Sophisticated SFC schemes for PEVs, for example using fuzzy logic or distributed data acquisition, have been reported to improve frequency stability [15], [16]. Supplementary SFC schemes were studied for the coordination of PEVs with other controllable loads [5], [17]. These studies showed the necessity of complex demand-side controllers to manage battery SOC levels, mainly because long-term variations existed in the supplementary SFC signals. It was shown in [18] that such variations exist in real SFC signals, thereby motivating the design of high-order filters to remove the DC offset.

The aforementioned papers analyzed the effects of DLC-enabled PEVs, mainly using trial-and-error approaches in a limited number of simulation case studies. The dynamic response of a real battery was seldom considered, and the gaps between academic research and industrial applications remain unresolved. The claimed performance of the GFR schemes requires further demonstration using experimental implementations. Furthermore, these papers did not consider the electric power system of a residential or commercial building. In [19], the effects of general V2G services on a building line capacity were estimated. In [20] and [21], the thermal dynamics of the rooms of buildings, instead of electrical system operations inside the building, were considered to analyze the ancillary service provision of thermal loads. The distribution of the DLC signal to individual electrical BESSs still needs to be comprehensively considered because their response times are significantly faster than those of thermal loads.

As the penetration of behind-the-meter BESSs continues to increase, ISOs will encounter difficulties in simultaneously controlling a number of small-scale BESSs [22]. A new type of electrical system in a building, as well as building-level and device-level controllers, will be necessary to achieve reliable ancillary service provision of behind-the-meter BESSs. In [23], we designed an electrical system for use in a commercial building, in which the coordination of the building-level controllers and the PEV charger controllers enabled the commercial building to act as an intermediate aggregator between the ISO and the multiple PEV owners and, consequently, to operate as a large-scale stationary BESS, particularly from the viewpoint of the ISO.

Using the building electrical system, this paper proposes a real-time GFR scheme, whereby the behind-the-meter BESSs compensate for rapid load variations through DLC, to reduce the frequency deviation and required reserve capacity of generators. The contributions of this paper are as follows:

- The low-pass filter (LPF) used in the proposed GFR scheme is much simpler than the high-order filters designed in [18]. It is used not only for segregation of the SFC signals but also for filtering of the frequency regulation signals.
- Various feedback controllers are considered for the SFC of the behind-the-meter BESSs. These controllers do not disturb the normal operation of the existing generators.

Therefore, it is expected that the proposed GFR can be implemented in practical power grids in an easy and safe manner.
- Few papers have included small-signal analyses for the frequency regulation of stationary or PEV batteries. In this paper, the proposed GFR scheme is comprehensively analyzed via small-signal analysis, particularly with respect to grid-level controllers for the behind-the-meter BESSs.
- Unlike the previous papers [5], [7]–[18], the proposed GFR is implemented using a laboratory-scale microgrid with a real DLC-enabled battery pack. Experimental studies prove that the objective of the proposed GFR scheme can be effectively achieved under various conditions.

Note that the proposed GFR scheme can be applied to general types of behind-the-meter BESSs such as wall-mounted battery packs, although Section II explains the electrical system model developed in [23], which particularly uses PEVs as the BESSs. Based on the model, Sections III-V analyze the proposed GFR via the small-signal analysis, the simulation case studies, and the experimental microgrid implementation, respectively.

II. DYNAMIC MODELING OF DLC-ENABLED BUILDING INCLUDING BEHIND-THE-METER BESSs

A new power system configuration inside a commercial building was developed in [23] to address the practical difficulties in the application of DLC, particularly in individual PEVs, which result from their limited battery power and energy capacities, and an increase in penetration [22]. Fig. 1(a) shows a simplified diagram of the DLC-enabled building, in which multiple PEVs are connected with a DC-link through charging stations, along with a rooftop PV generator and conventional building loads. The conventional loads, such as lights and refrigerators, have little influence on the dynamic response of the PEVs to DLC signals; therefore, they are modeled as ZIP loads for simplicity. An AC-DC bidirectional converter is used as the interface between the DC-link and the utility grid. This enables the building to act as a large-scale inverter-interfaced stationary BESS, especially from the viewpoint of the ISO. Fig. 1(b) shows a comprehensive diagram including building-level and device-level controllers for the DC units in the building.

The rated battery capacities were set to 16 kWh, 18 kWh, and 20 kWh, based on [24]. The rated power capacity of the PEV charger was 45 kW, determined from the data obtained using the DC charging method [24] and the Level 3 equipment [25]. As shown in Fig. 2(a), the PEV battery was modeled using a controlled voltage source, and its internal voltage was calculated using the equations provided in [26]. The battery model was then verified using a comparison of the discharging curve with that of the experimental battery described in [27], as shown in Fig. 3. In this study, a variable-current and constant-voltage (VC-CV) charging scheme was developed, as shown in Fig. 2(b), to both prevent overvoltage and provide a real-time GFR ancillary service.

The participation of the commercial building in real-time GFR is achieved by adjusting the total instantaneous input power (i.e., $P_{\text{tot\_ev}} = \sum_k P_{\text{ev}}^k$.) of the PEVs in response to
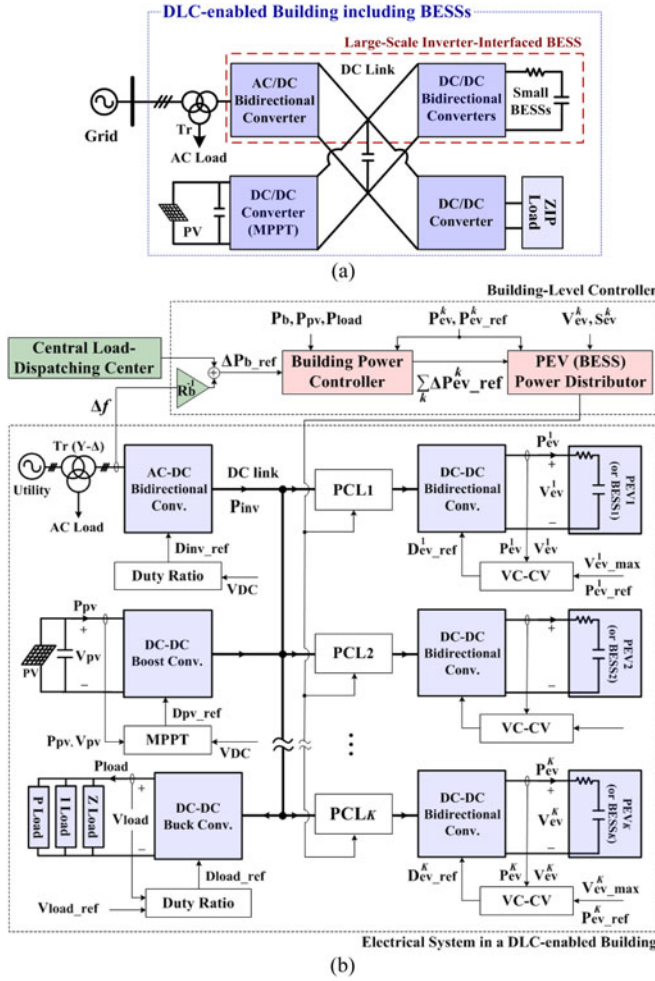
Fig. 1. (a) Simplified and (b) comprehensive schematic diagrams of the proposed electrical system inside a commercial building.
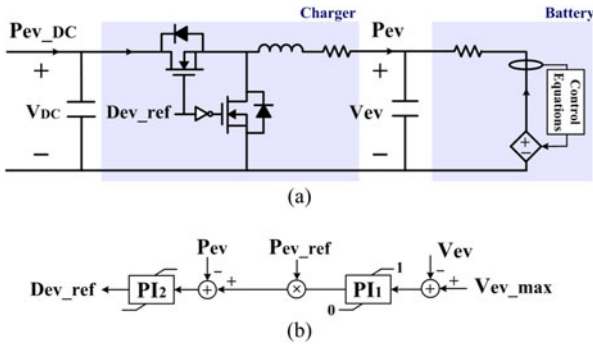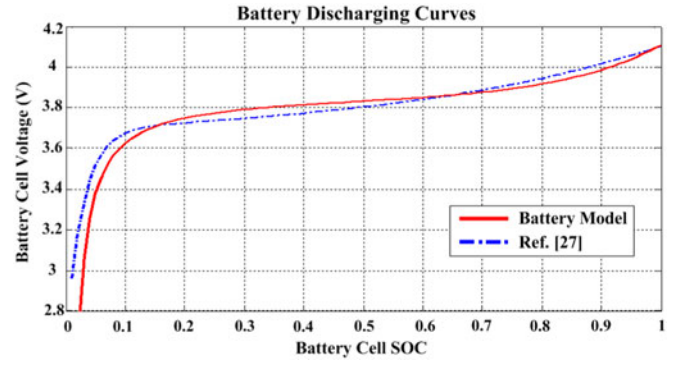

Fig. 3. Comparison of the discharge curves of the battery model used in Fig. 2 and the one designed using the experimental data in [27].
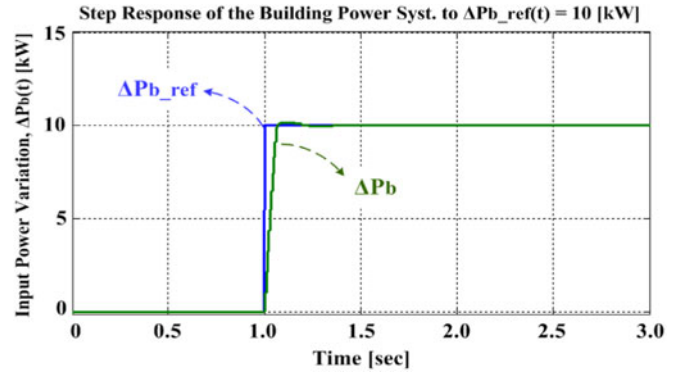

Fig. 4. Step response of the DLC-enabled building to $\Delta P_{b\_\mathrm{ref}}(t = 1^+) = 10$ kW.

Fig. 2. (a) PEV battery and charger model and (b) a VC-CV charging controller.

$\Delta P_{b\_\mathrm{ref}}$, which consists of PFC and SFC signals. In Fig. 1(b), the Building Power Controller (BPC) measures the frequency deviation Δf to support PFC, and receives SFC signals from the central load-dispatching center. Based on the PEV battery voltage V_{ev}^k and SOC S_{ev}^k, the PEV Power Distributor (PPD) then distributes $\Delta P_{b\_\mathrm{ref}}$ to the individual PEVs that are connected to the building power lines. The coordinated operation of the

BPC, the PPD, and the VC-CV controllers was developed to enable the DLC-enabled building to follow $\Delta P_{b\_\mathrm{ref}}$ successfully, while charging the batteries and compensating for rooftop PV power fluctuations [23]. In this manner, the building is considered as a stationary DLC-enabled BESS, from the viewpoint of the ISO, such that the effects of PEV mobility on GFR can be mitigated. This is further explained in Appendix A; however, sophisticated forecasting schemes to statistically estimate PEV driving patterns are not discussed in this paper.

Fig. 4 shows the step response of the building-power-system model to a 10-kW increase in the input power reference P_{b_ref} at $t = 1$ s (i.e., $\Delta P_{b\_\mathrm{ref}}(t = 1^+) = 10$ kW). Fig. 4 shows that the DLC-enabled building can respond within a short period, so that ΔP_b is adjusted to follow the DLC signal $\Delta P_{b\_\mathrm{ref}}$ after approximately 0.07 s for the 10-kW step variation. This fast response is attributed to the inverter interfaces of the BESSs.

Parking lots can also play the role of an aggregator between an ISO and PEVs. The building-electrical-system model shown in Fig. 1 can provide a basis for control schemes of parking lots. The building model can be applied to both PEVs in a building garage and wall-mounted BESSs installed inside various types of buildings, such as data centers.
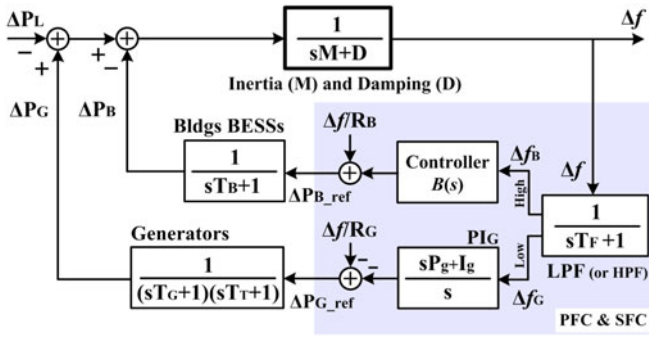
Fig. 5.   Block diagram for the small-signal frequency-domain analysis of the proposed GFR in an isolated grid with the DLC-enabled buildings.
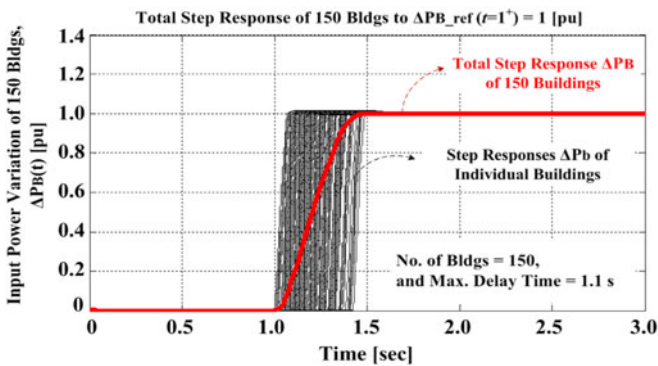

Fig. 6.   Total step response of 150 DLC-enabled buildings for $t_{\max} = 1.1$ s.

III. SMALL-SIGNAL ANALYSIS OF DLC-ENABLED BUILDINGS

Fig. 5 shows a simplified block diagram of the proposed GFR scheme in an isolated power grid along with the DLC-enabled behind-the-meter BESSs. The generators compensate for the low-frequency components of Δf, whereas the behind-the-meter BESSs compensate for the high-frequency components. The following conditions were also considered:

- The total dynamic response of the generators using non-reheat turbines can be represented by a second-order transfer function [29], [30]. The analysis of various types of generators is left for future work.
- The first-order response of the aggregated buildings distributed over a wide range of locations is attributable to random time delays in communications links [30], [31]. The DLC signal ΔP_{B_ref} was assumed to arrive at the individual buildings with random time delays that were uniformly distributed in the range 0 to $t_{\max}$ [31]. Fig. 6 shows the first-order dynamic response of 150 buildings for $t_{\max} = 1.1$ s.
- The reference signals ΔP_{G_ref} and ΔP_{B_ref} for the GFR consist of two components, which correspond to PFC and SFC signals, respectively. The PFC signals are continuously produced using proportional (P) controllers at locations where the individual buildings are connected to the grid. The SFC signals are updated and delivered

from the ISO to the buildings every 2 s, and consequently to the BESSs.
- Based on the available FRR capacities of generators and buildings, the ISO determines the maximum magnitudes and variations in ΔP_{G_ref} and ΔP_{B_ref} by setting R_G and R_B, as well as the gains of PI_G and $B(s)$ [32]–[35].

In addition, a proportional-integral (PI) controller is typically adopted for SFC of generators in real power grids, whereas the controller $B(s)$ for the buildings has not yet been specified in the grid operating standards or regulations. In this paper, three controllers, widely used for feedback control, were taken into consideration for the proposed GFR as described in (1)–(3):

$$\bullet \text{PI}: B_1(s) = \left(P_b + \frac{I_b}{s} \right), \tag{1}$$

$$\bullet \text{PID}: B_2(s) = \left(P_b + \frac{I_b}{s} + D_b s \frac{N_1}{s + N_1} \right), \quad \text{and} \tag{2}$$

- PID with a phase-lead compensator (LC-PID):

$$B_3(s) = \left(P_b + \frac{I_b}{s} + D_b s \frac{N_1}{s + N_1} \right) \cdot \left(\frac{N_4 s + N_3}{s + N_2} \right). \tag{3}$$

Note the differential (D) controller in (2), which can effectively prevent undesirable noises in high-frequency ranges. The lead-compensated PID (LC-PID) controller in (3) is a PID controller cascaded with a phase-lead compensator to increase the gain $B(s)$ from +20 dB/dec to +40 dB/dec in the target frequency range [36]. In practice, (2) and (3) should be carefully implemented considering the noise in control signals.

The time constant of the LPF was set to $T_F = 0.573$ s, based on the analysis in [18], where the power spectral density curves of real frequency regulation power signals are extended to approximately 10^3 cycles/h. A rather conservative estimate of T_F was used, primarily to avoid disturbing the operation of the existing generators. In response to load demand variation ΔP_L, Δf can then be determined in the proposed GFR as follows:

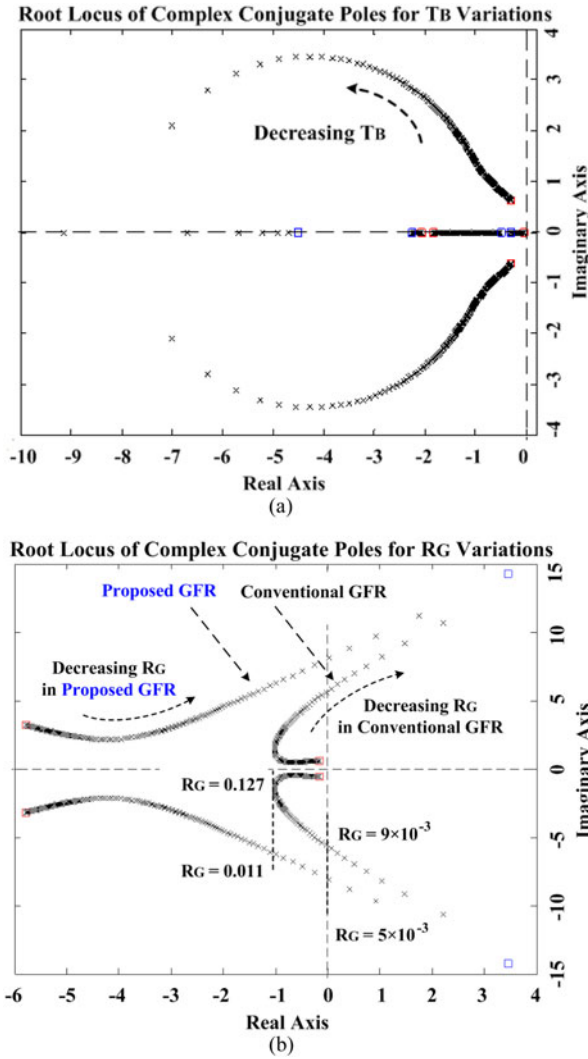$$\frac{\Delta f(s)}{\Delta P_L(s)} = \frac{-1}{(sM + D) + (sT_B + 1)^{-1} \ell_1(s) + \ell_2(s)} \tag{4}$$

where

$$\ell_1(s) = \frac{sT_F}{sT_F + 1} B(s) + \frac{1}{R_B}, \quad \text{and} \tag{5}$$

$$\ell_2(s) = \frac{1}{(sT_G + 1)(sT_T + 1)} \left\{ \frac{sP_g + I_g}{s(sT_F + 1)} + \frac{1}{R_G} \right\}. \tag{6}$$

For the conventional GFR, $\ell_1(s)$ and T_F are set to zero. In the t-domain, state-space equations equivalent to (4)–(6) can be developed as discussed for a feedback system in [37].

Fig. 7 shows a comparison of pole-zero plots of the closed-loop transfer functions given by (4) using the numerical per-unit values provided in [29] and [38]. For the proposed GFR, the PI controller in (1) was used for $B(s)$. In the proposed GFR, the complex-conjugate pole pair was located farther away from the imaginary axis than in the conventional one. It follows that the smaller magnitude of Δf in the proposed GFR arises from the imbalance between ΔP_G and ΔP_L.
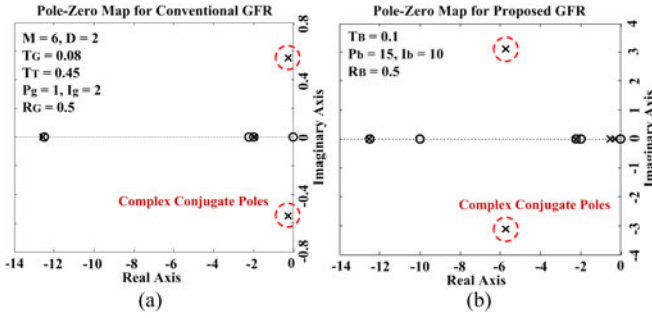
Fig. 7.   Pole-zero plots of $\Delta f / \Delta P_L$: (a) conventional and (b) proposed GFR.

Fig. 9.   Bode plot diagrams of $\Delta f / \Delta P_L$ for the conventional and proposed GFR.

Fig. 8.   Root locus of the complex-conjugate pole pair for variations in the parameters (a) T_B and (b) R_G.

As the time constant of building BESSs T_B becomes small, the complex-conjugate pole pair moves away from the imaginary axis, as shown in Fig. 8(a). Such separation from the imaginary axis cannot be achieved by decreasing the droop constant R_G of the generators in the conventional GFR. An excessive decrease in R_G will lead to network instability, as shown in
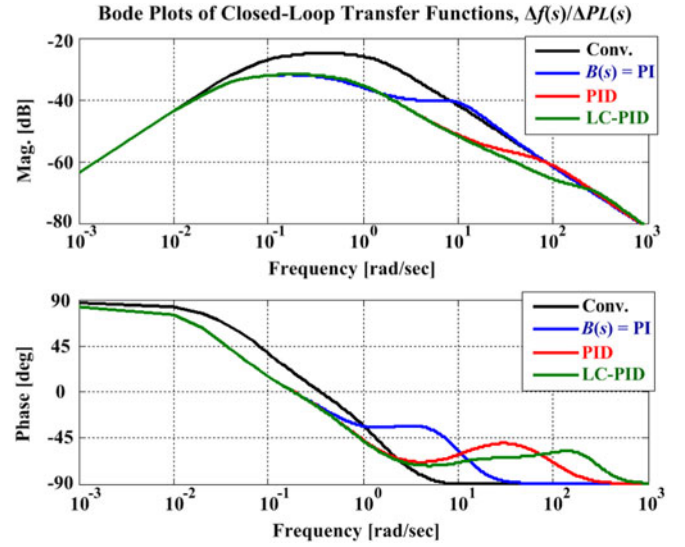
Fig. 8(b), in which the pole pair moves away slightly from the imaginary axis, but changes direction toward the right-hand half plane. Similar movements of the pole pair were also observed with increases in P_g and I_g of the generators.

Fig. 9 shows the band-pass-filter characteristics of (4), mainly because the SFC of generators is achieved using an int-egral (I) controller. The effects of different $B(s)$ (i.e., (1)–(3)) on the closed-loop transfer functions were also investigated for the proposed GFR scheme in Fig. 9. For all $B(s)$, the proposed GFR is effective in improving the grid frequency stability. The DLC-enabled buildings result in a smaller magnitude of (4), especially, for s greater than the cut-off frequency $s_0 = j|D/M|$, whereas the rotary generators normally compensate for the slow load demand variations for s lower than $s_0 = j|D/M|$. Therefore, the proposed GFR ensures the normal operation of the generators. For the load variation ΔP_L, Δf is attenuated most significantly when the LC-PID controller is used for $B(s)$. Fig. 9 shows that the proposed GFR ensures passivity in the power system operation (i.e., stability, with the phase of the Bode plot remaining within $\pm 90°$).

To design $B(s)$, the ISO is assumed to be aware of the parameters: M, D, R_G, P_g, and I_g. This is necessary even for current GFR operations. It follows that the proposed GFR does not require more information on generators than the conventional GFR or other methods discussed in [14]–[16]. Fig. 10 shows the variations in $|\Delta f(s)/\Delta P_L(s)|$ for the conventional GFR, based on M, D, R_G, P_g, and I_g. From Fig. 10, P_b and I_b can be easily determined, as shown in Fig. 11(a), by gradually increasing P_b, and hence I_b. Rather than the transfer function parameters (i.e., T_G, T_T, and T_B), the PFC and SFC gains of the generators have a direct influence on P_b and I_b. Note that the buildings act as a damping resistor that prevents undesirable resonances in an electric circuit. Similarly, D_b can be determined based on the target frequency range of $s_3 \leq s \leq s_4$, as shown in Fig. 11(b) where D_b and N_1 are equal to $P_b/|s_3|$ and $|s_4|$, respectively.
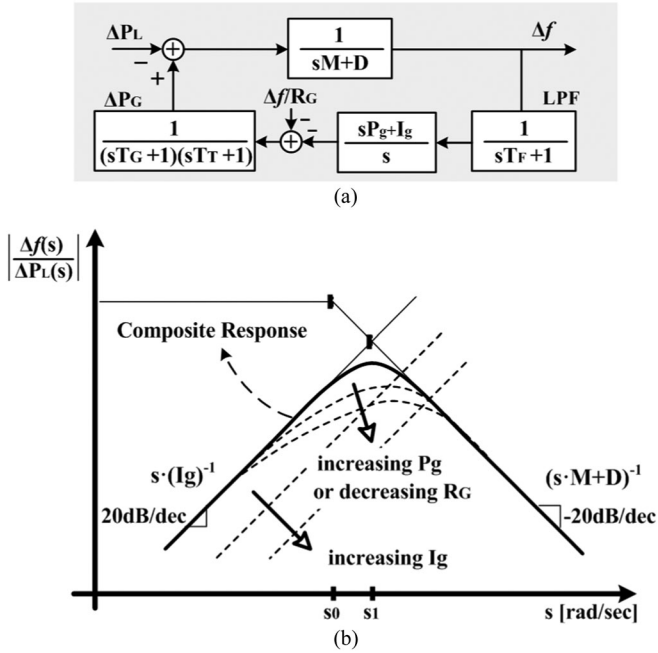
Fig. 10. (a) Block diagram for the conventional GFR and (b) variations in the corresponding $|\Delta f(s)/\Delta P_L(s)1/2|$.

Fig. 11. Variations in $|\Delta f(s)/\Delta P_L(s)1/2|$ in the proposed GFR for (a) a PI controller, (b) a PID controller, and (c) an LC-PID controller used as $B(s)$.

In Fig. 11(c), an LC-PID controller decreases $|\Delta f(s)/\Delta P_L(s)|$ from -20 dB/dec to -40 dB/dec in the frequency range of $s_3 \leq s_5 \leq s \leq s_6 \leq s_4$. Using the Bode plot of the compensator, N_2, N_3, and N_4 can be set to $|s_6|$, $N_2 DC_{\mathrm{gain}}$, and $N_3/|s_5|$, respectively. The DC gain of the lead compensator DC_{gain} can be determined based on $(sM + D)^{-1}$ in the target frequency range.

IV. SIMULATION CASE STUDIES AND RESULTS

A. Test System and Simulation Conditions

The effects of the DLC-enabled behind-the-meter BESSs on frequency stability were analyzed using the test grid shown in Fig. 12, which was modeled using the IEEE 34-node test feeder [39], with small modifications based on [28] and [40]. The test grid capacity was set to 25 MVA. Table I lists the detailed specifications of the test grid. The output power of the PV system was sampled at one second intervals and scaled up such that the total maximum output power was 1 MW, as shown in Fig. 13(a). Fig. 13(b) shows the total load demand in the grid.

The comprehensive model of the DLC-enabled building shown in Fig. 1(b) was directly used in the test grid for simulation studies. For simplicity, we assumed the existence of two types of DLC-enabled buildings, where the rated capacities of the batteries and chargers, as well as the steady-state building loads, differed. The load demand for each type of building was then scaled up, such that the blue points for Bldgs$_1$ and Bldgs$_2$, shown in Fig. 12, represent a group of buildings having the same load profiles. The DLC signal assigned to each group of buildings was delivered to the individual buildings with random
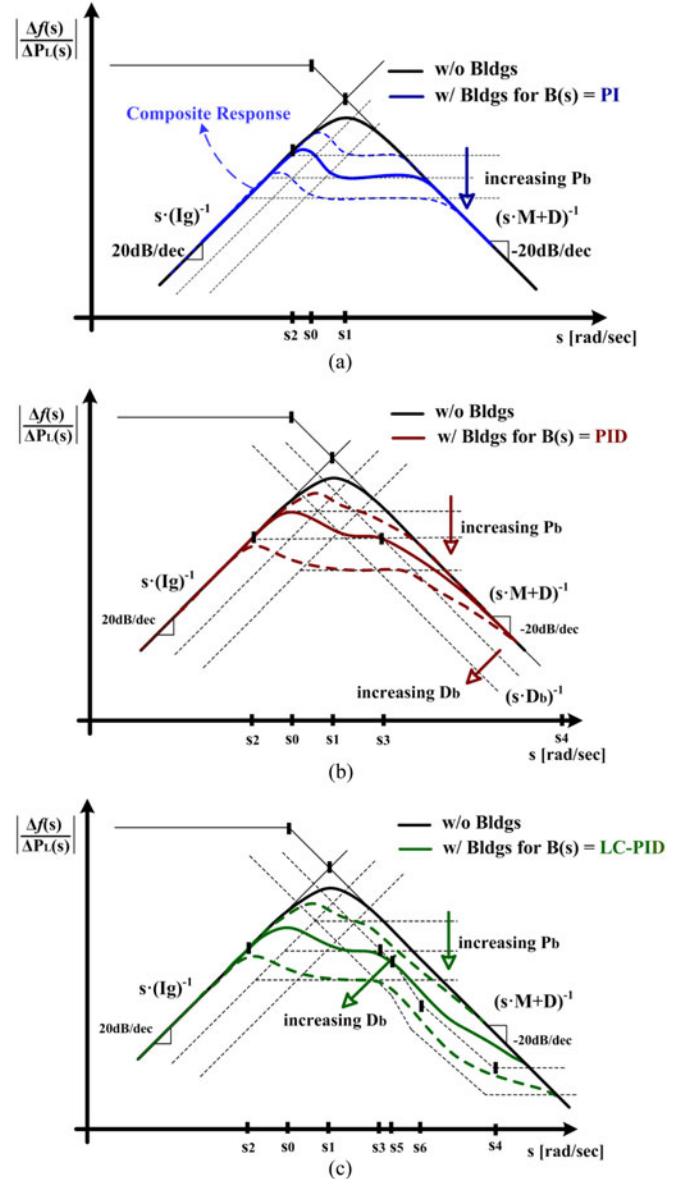
communication delays that were uniformly distributed between 0 s and $t_{\mathrm{max}} = 1.1$ s.

The proposed GFR scheme can be expressed in the frequency domain as shown in Fig. 14, where the ISO measures the real-time grid frequency, calculates the target power to maintain the nominal frequency, and sends the regulation signals to the distributed generators (DGs) and the groups of buildings via the PFC and SFC feedback loops. For the isolated grid, the target power is calculated using the frequency deviations only; however, the proposed GFR is still effective in interconnected power systems. The LPF was used for both the filtering and segregation of the SFC signals. For simplicity, the DLC signals $\Delta P_{B\_\mathrm{ref}}$ were assumed to be distributed equally among the individual buildings. Based on the FRR capacities of the individual DLC-enabled buildings, $\Delta P_{B\_\mathrm{ref}}$ can be optimally distributed
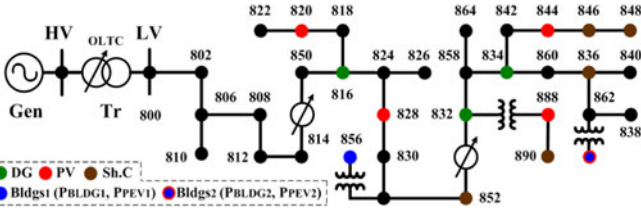
Fig. 12.   Single-line diagram of the isolated test grid.

TABLE I
DETAILED SPECIFICATIONS OF THE TEST GRID

|	
DGs	HV side: $P_{\text{rated}} = 15$ MW to compensate for 5-min load variation
	LV side: $P_{\text{rated}} = 3.5$ MW (816), 2.5 MW (832), and 3.0 MW (834)
PV	Total $P_{\text{peak}} = 1$ MW as the scaled-up output of the real PV system, which was measured at one second intervals, as shown in Fig. 13(a)
Loads	Balanced loads from 15.80 MW to 19.01 MW reflecting the scaled-up RegD signals in [40], as shown in Fig. 13(b) (0.85 pf lag)
Bldgs	Maximum building load demand of 530 kW in an individual building in Bldgs$_1$ (856) or Bldgs$_2$ (866)
Tr	3-phase, 115/69 kV, 25 MVA, $x = 8\%$, $x/r = 20$
	On-load tap changer for -10% to $+10\%$ voltage regulation
Sh.Cs	1.5 Mvar each for (836), (848), and (890)
	1 Mvar each for (846) and (852)
D/Ls	Balanced line impedances adopted from the average values of each line configuration in [39]
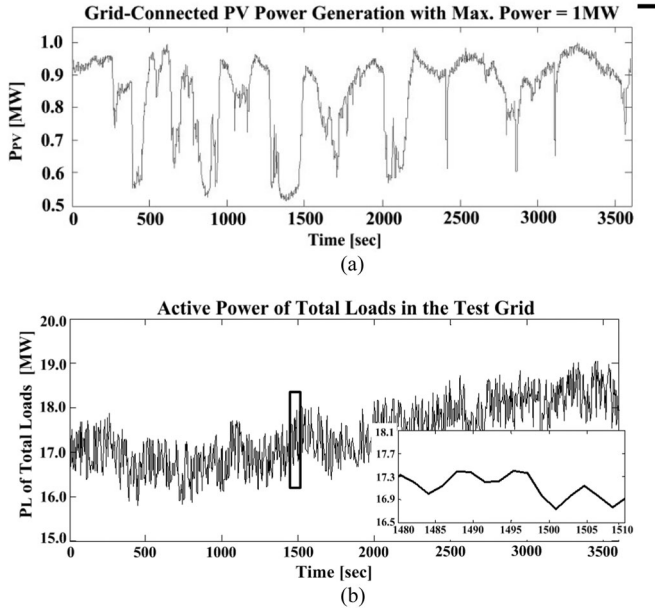
Fig. 13.   (a) The total PV generator output power and (b) the total grid load.

to achieve various objectives in a scheduling time horizon; for simplicity, this is not considered further here. The DG responses $\Delta P_{G1,...,NG}$ to the regulation signals were calculated using the lumped models discussed in Section III, whereas the responses of the building BESSs $\Delta P_{B1,...,NB}$ were obtained using the comprehensive building model shown in Fig. 1(b). In Fig. 14, nonlinear functions for time delay, dead band, ramp-rate limi-
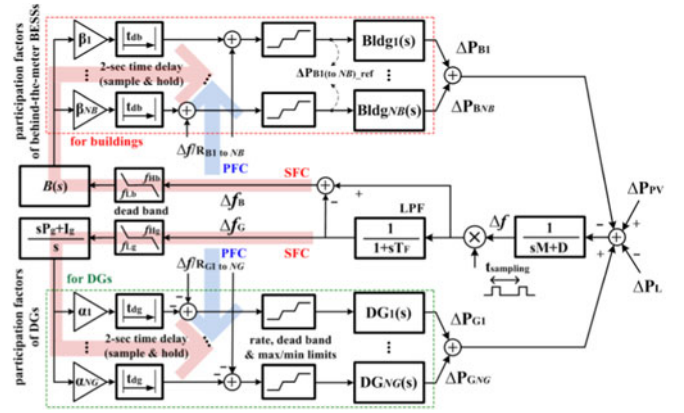

Fig. 14.   Comprehensive block diagram of the proposed GFR for the test grid.

TABLE II
PARAMETERS FOR CASE STUDIES USING THE PROPOSED GFR SCHEME

Inertia and load damping in the test grid		
M	6	
D	1	
DGs		
$DG_{1,2,3}$ (s)	$\dfrac{e^{-0.5s}}{(0.22s+1)(0.35s+1)}$, $\dfrac{e^{-0.6s}}{(0.25s+1)(0.37s+1)}$, $\dfrac{e^{-0.55s}}{(0.26s+1)(0.33s+1)}$	
$R_{G1,2,3}$	0.35, 0.30, and 0.33	
$\alpha_{1,2,3}$	0.3838, 0.3030, and 0.3132	
P_g, I_g	1 and 2	
t_{dg}	2 s	
f_{Hg}, f_{Lg}	± 0.005	
DLC-enabled buildings		
$R_{B1,2}$	0.26 and 0.24	
$\beta_{1,2}$	0.5833 and 0.4167	
P_b, I_b	25 and 10	
max. ΔP_{b_ref}	$\pm 10\%$ of the total rated power of BESS chargers in the building	
t_{db}	2 s	
f_{Hb}, f_{Lb}	± 0.003	

tation, and maximum/minimum saturations are also considered to emulate a practical GFR scheme.

The ISO is assumed to have information on the scheduled DG power generation, the building power consumption, and their available FRR capacities, so that it can determine the participation factors (i.e., α_{1-NG} and β_{1-NB}) and the PFC and SFC gains (i.e., R_G, R_B, P_g, I_g, P_b, and I_b), as shown in Fig. 14. Table II lists the parameters used in the proposed GFR scheme shown in Fig. 14; apart from $B(s)$, the parameter values were determined based on the existing simulation case studies provided in [5], [8], [9], [11], [12], and [14]–[16]. In addition, Table III specifies the given constants and the ISO's control variables. In the proposed GFR, the DLC application has little influence on the SOC levels of the behind-the-meter BESSs, and therefore the participation factors and controller gains will not have to change significantly in real time. Furthermore, in general, high market prices for ancillary services are expected to increase the FRR capacities that are available for the GFR; for simplicity, the effects of market prices, as well as weather conditions, are not considered further in this paper.

TABLE III
TYPES OF MAIN VARIABLES USED FOR THE PROPOSED GFR SCHEME

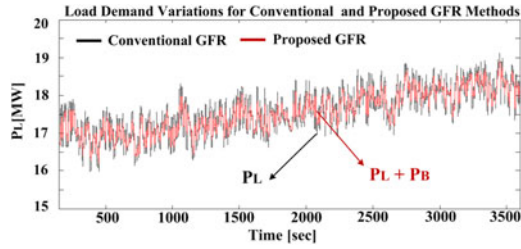| Variables	Types	Variables	Types
M, D	Given	P_b, I_b, D_b, N_{1-4}	ISO
T_G, T_T, T_B, T_F	Given	t_{dg}, t_{db}	ISO or Given
$R_G, R_B, \alpha_{1-NG}, \beta_{1-NB}$	ISO	$f_{Hg}, f_{Lg}, f_{Hb}, f_{Lb}$	ISO
M, N	Given	P_{b_max}	Given
P_g, I_g	ISO	ΔP_{b_ref}	ISO

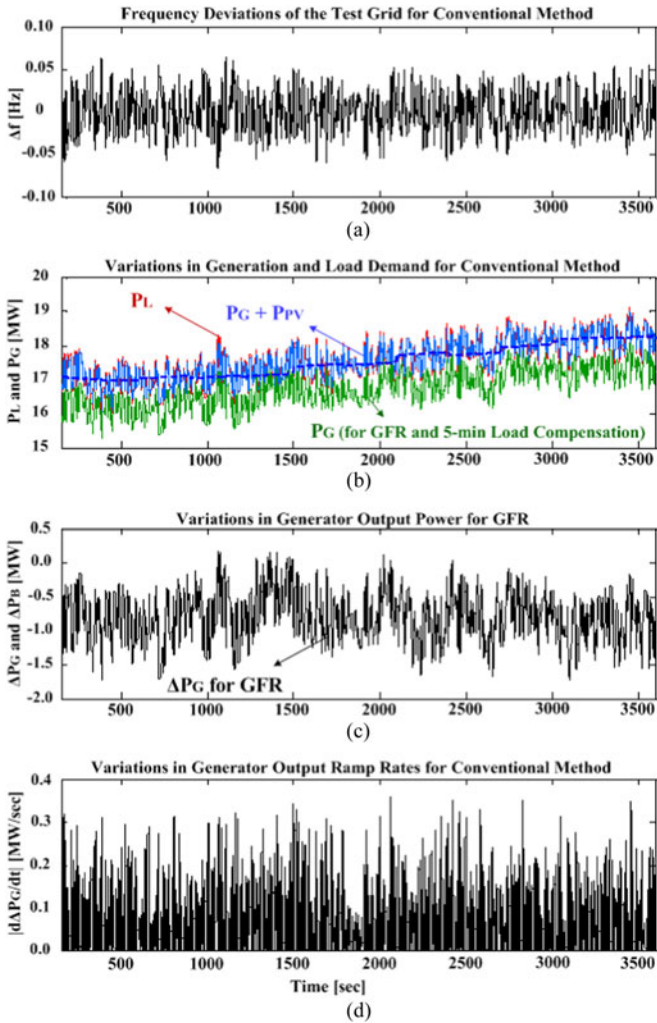Fig. 15.   Reduced variation in the load demand for the proposed GFR method.

Fig. 16.   Simulation case study results for the conventional GFR methods:
(a) Δf, (b) P_L, P_G, and $P_G + P_{PV}$, (c) ΔP_G, and (d) $|d\Delta P_G/dt1/2|$.
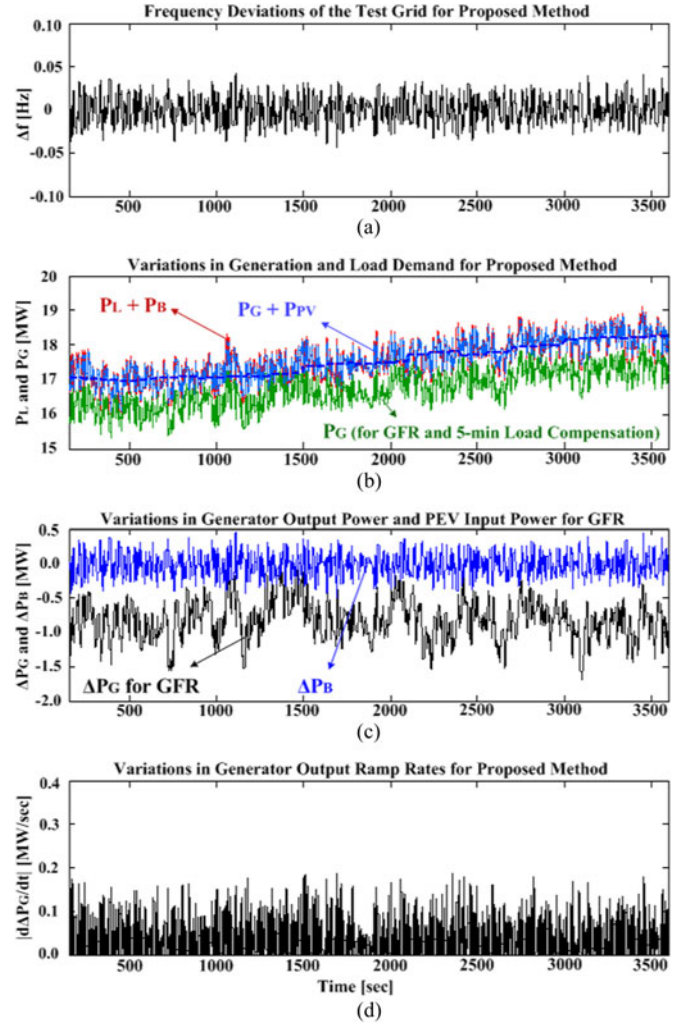

Fig. 17.   Simulation case study results for the proposed GFR methods:
(a) Δf, (b) $P_L + P_B$, P_G, and $P_G + P_{PV}$, (c) ΔP_G and ΔP_B, and
(d) $|d\Delta P_G/dt1/2|$.

B. Simulation Case Study Results

In the proposed GFR scheme, the behind-the-meter BESSs
in the DLC-enabled buildings can successfully compensate for
the high-frequency components of the variations in the load
demand, as shown in Fig. 15. Figs. 16 and 17 show the simula-
tion case study results for the conventional and proposed GFR
schemes, respectively. The proposed GFR method shows a de-
crease in grid frequency deviation (i.e., Δf in Fig. 17(a)) and
the output power variation of the DGs participating in the GFR
(i.e., ΔP_G in Fig. 17(c)), when compared to the conventional
method (see Fig. 16(a) and (c)). Figs. 16(b) and 17(b) show the
total output power of the DGs and the PV generators, as well
as the load demand, for the conventional and proposed meth-
ods, respectively. Comparing Figs. 16(d) and 17(d) shows that
the proposed GFR method led to smaller generation ramp-rates
$|d\Delta P_G/dt|$ than the conventional method.

For statistical comparison, one-hour simulation studies were
performed iteratively, where the magnitude and variation of
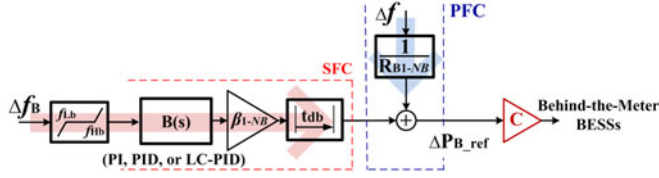ΔP_{B_ref} were gradually increased; i.e., the PFC and SFC gains

Fig. 18. Increase in the magnitude and variation of the DLC signals to analyze the effects of behind-the-meter BESS penetration.

for the behind-the-meter BESSs were increased by a constant factor C, as shown in Fig. 18. This is equivalent to an increase in the penetration of BESSs that are able to respond to ΔP_{B_ref}. The time-domain data obtained from the iterative case studies were then processed, to calculate Δf, $d\Delta P_G/dt$, ΔP_{G_max}, and *std.* ΔP_B for different values of C.

Fig. 19(a) and (b) show the peak-to-peak and RMS variations in the frequency—$\Delta f_{peak-to-peak}$ and Δf_{rms}, respectively, for various values of the standard deviation of the BESS input power *std.* ΔP_B. Fig. 19(c) and (d) represent the average and maximum ramp-rates of the DG generation—*avg.* $d\Delta P_G/dt$ and max. $d\Delta P_G/dt$, respectively. Fig. 19(e) and (f) give the maximum variations in the total DG output and BESS input power—ΔP_{G_max} and ΔP_{B_max}, respectively. As *std.* ΔP_B was increased, $\Delta f_{peak-to-peak}$, Δf_{rms}, *avg.* $d\Delta P_G/dt$, max. $d\Delta P_G/dt$, and ΔP_{G_max} were effectively reduced for all $B(s)$ in the proposed GFR scheme, until they reached their saturation points. The linear decrease in these values as *std.* ΔP_B increases can also be explained using the analysis described in Section III.

In particular, ΔP_{G_max} was decreased by approximately 35% for the proposed GFR scheme at *std.* $\Delta P_B = 55.6$ kW when saturation started to occur. Since the FRR requirement is dependent on ΔP_{G_max} and $d\Delta P_G/dt$ [28], [41], the DG operating cost is expected to be reduced in the proposed GFR method; the corresponding cost-benefit analysis requires significant work and therefore will be addressed in future studies.

V. EXPERIMENTAL CASE STUDIES AND RESULTS

A. Experimental Implementation of the Test Grid

The test grid shown in Fig. 12 was implemented in a laboratory-scale microgrid, shown in Fig. 20. It included a 27-kVA three-phase generator emulator, a 5-kVA load emulator, a 4-kVA inverter-interfaced Li-ion battery pack, and a 15-kW resistive heater. The generator emulator was implemented as a variable-frequency voltage source. The dynamic response of the generator emulator was programmed using a simulation model to represent the total response characteristics of the DGs at the HV and LV sides, as well as the aggregated frequency-sensitive loads in the test grid. In this manner, the frequency deviation was determined based on the instantaneous imbalance between generation and load demand, and the variable frequency drive of the generator emulator then adjusted the voltage frequency. The heater and the load emulator were used as the base and peak loads, respectively.
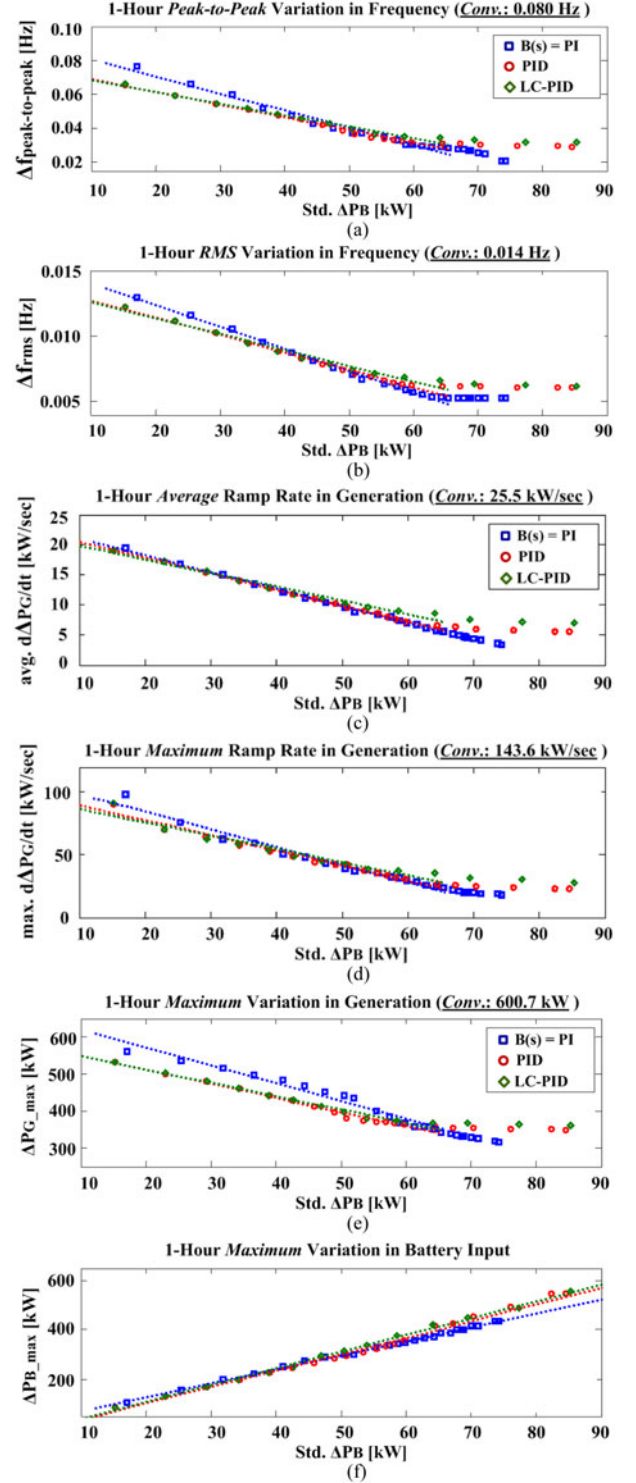

Fig. 19. (a) $\Delta f_{peak-to-peak}$, (b) Δf_{rms}, (c) *avg.* $d\Delta P_G/dt$, (d) max. $d\Delta P_G/dt$, (e) ΔP_{G_max}, and (f) ΔP_{B_max} in the test grid due to the proposed GFR.

The battery pack was connected to the microgrid via an AC-DC converter and a DC-DC buck-boost converter in a back-to-back configuration. The converter topologies are the same as those in the model of the DLC-enabled building discussed in Section II. The configuration is also consistent with the interfaces of the PEVs in the building as shown in Fig. 1(a). For
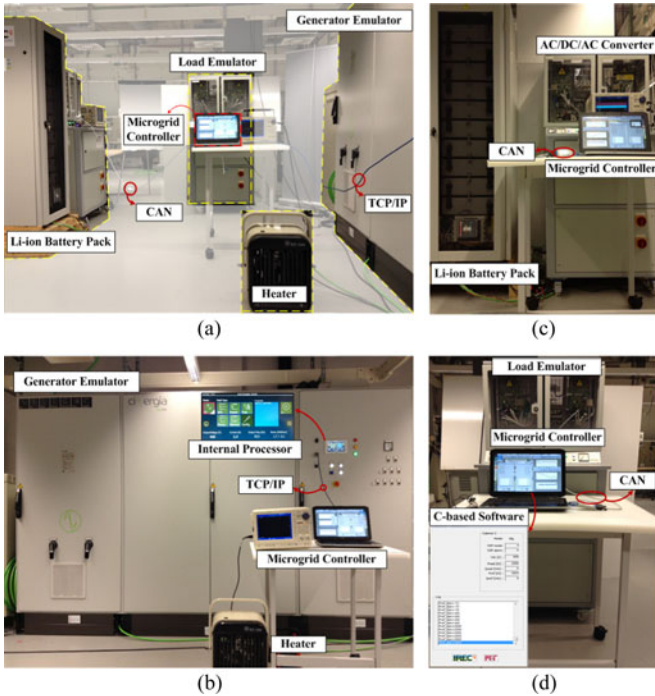
Fig. 20. (a) Experimental setup for the implementation of the test grid including (b) a generator emulator, (c) a Li-ion battery pack, and (d) a load emulator.
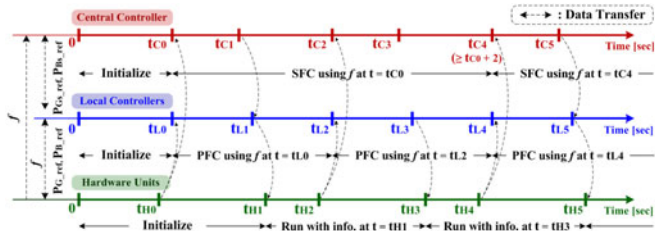

Fig. 21. Real-time reference and measured signal transfer for PFC and SFC of the generator emulator and the DLC-enabled battery pack.

the experimental studies, the duty ratios of the battery converter were controlled to emulate (7), which is equivalent to the total dynamic response of the aggregated DLC-enabled behind-the-meter BESSs. The first-order transfer function (7) is also consistent with the simulation models in [5], [38], and [42].

$$\frac{\Delta P_B(s)}{\Delta P_{B\_\text{ref}}(s)} = \frac{1}{sT_B + 1}. \tag{7}$$

As shown in Fig. 21, the microgrid control centers were developed for real-time communication with the hardware units. The SFC signals were produced in the central controller every 2 s based on the grid frequency measured at the generator emulator. The signals were then delivered to the local controllers and from there, to the hardware units. The PFC signals were transmitted directly to the hardware units.

Fig. 22 shows the dynamic responses of the battery and the generator emulator to the reference signal variations. In Fig. 22(a) and (b), the inverter-interfaced battery pack had fast dynamic responses, to follow the DLC signal variations successfully. The step response demonstrates that the battery pack was
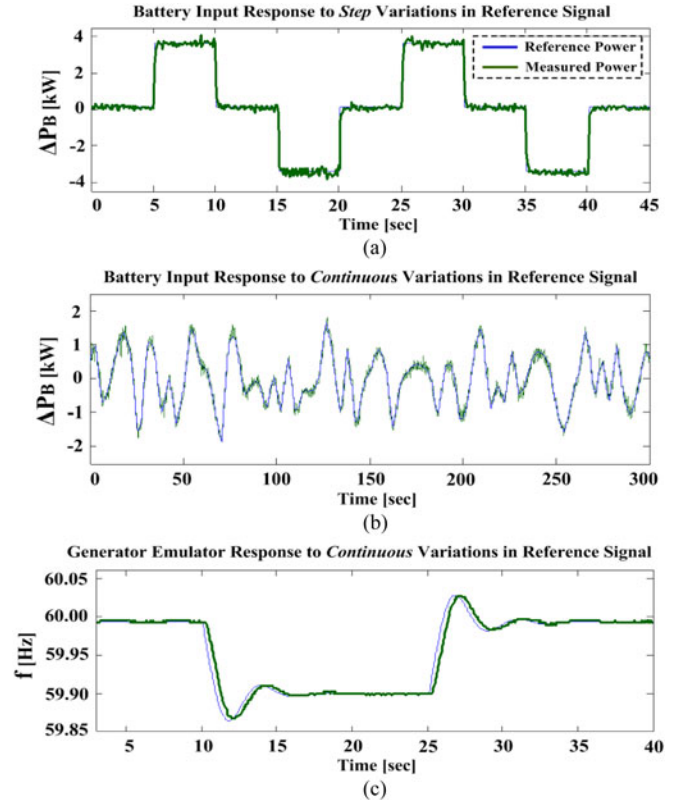

Fig. 22. (a) Step and (b) continuous responses of the battery pack and (c) continuous response of the generator emulator to the reference signal variations.

capable of emulating the total dynamic response given by (7) of the aggregated building BESSs in the experimental studies, and not just verifying the dynamic response of the DLC-enabled building shown in Fig. 4. Fig. 22(c) represents the frequency responses to step load variations of ± 0.05 pu when the generator emulator was equipped with a droop controller in the conventional GFR scheme. The response is commonly observed in a practical grid model [43].

B. Experimental Case Study Results

Figs. 23 and 24 show the frequency and generator responses to the step variations in the load demand for the conventional and proposed GFR schemes, respectively. For the proposed GFR, the PI controller was used for $B(s)$. In particular, the behind-the-meter BESSs decreased Δf by compensating for the high-frequency components of the load demand variations. This allowed the DGs to change their output power slowly while maintaining Δf within ± 0.05 Hz, which consequently decreased both $avg.\ d\Delta P_G/dt$, $\max.\ d\Delta P_G/dt$, and $\Delta P_{G\_\max}$. As shown in Table IV, the DLC-enabled buildings effectively reduced all the comparison terms (a)–(e) in the proposed GFR scheme. The percentages describe the decrease in each comparison term. In particular, $B(s)$ using the PID and LC-PID controllers produced slightly lower values of $d\Delta P_G/dt$.

Analogous to Fig. 19, Fig. 25 shows the results of one-hour experimental case studies performed while gradually
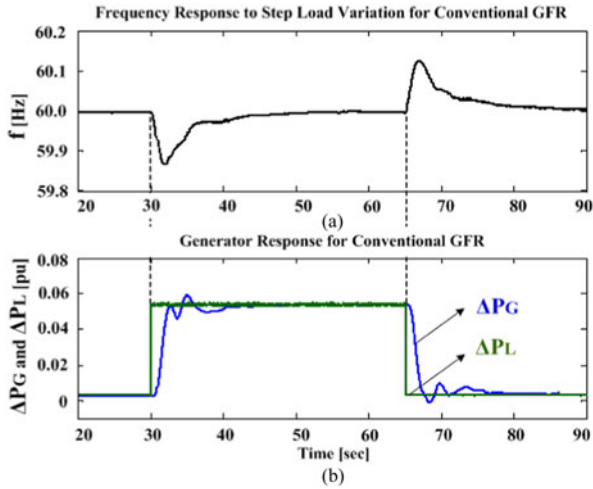
Fig. 23. (a) The frequency and (b) generation responses to the step variations of ± 0.05pu in the load demand for the conventional GFR.
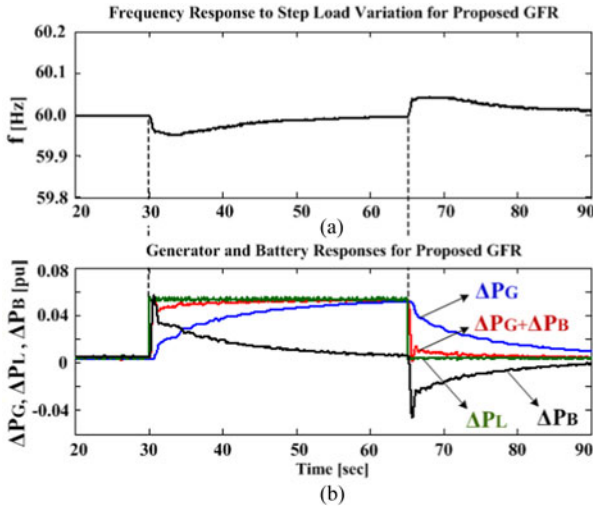

Fig. 24. (a) The frequency and (b) generation responses for the proposed GFR.

TABLE IV
COMPARISONS OF CONVENTIONAL AND PROPOSED GFR SCHEMES

Comparison Factors	Unit	Conventional GFR	Proposed GFR		
			$B(s)=$ PI	PID	LC-PID
(a) $\Delta f_{\mathrm{peak-to-peak}}$	Hz	2.58×10^{-1}	9.09×10^{-2} (64.75%)	8.99×10^{-2} (65.15%)	8.99×10^{-2} (65.15%)
(b) Δf_{rms}	Hz	2.91×10^{-2}	1.86×10^{-2} (36.08%)	1.83×10^{-2} (37.11%)	1.83×10^{-2} (37.11%)
(c) *avg.* $d\Delta P_{\mathrm{G}}/dt$	pu/sec	1.53×10^{-3}	9.01×10^{-4} (41.11%)	8.86×10^{-4} (42.09%)	8.84×10^{-4} (42.22%)
(d) max. $d\Delta P_{\mathrm{G}}/dt$	pu/sec	3.79×10^{-2}	2.31×10^{-2} (39.05%)	1.75×10^{-2} (53.83%)	1.74×10^{-2} (54.09%)
(e) $\Delta P_{G\_\mathrm{max}}$	pu	5.99×10^{-2}	4.89×10^{-2} (18.36%)	4.89×10^{-2} (18.36%)	4.89×10^{-2} (18.36%)
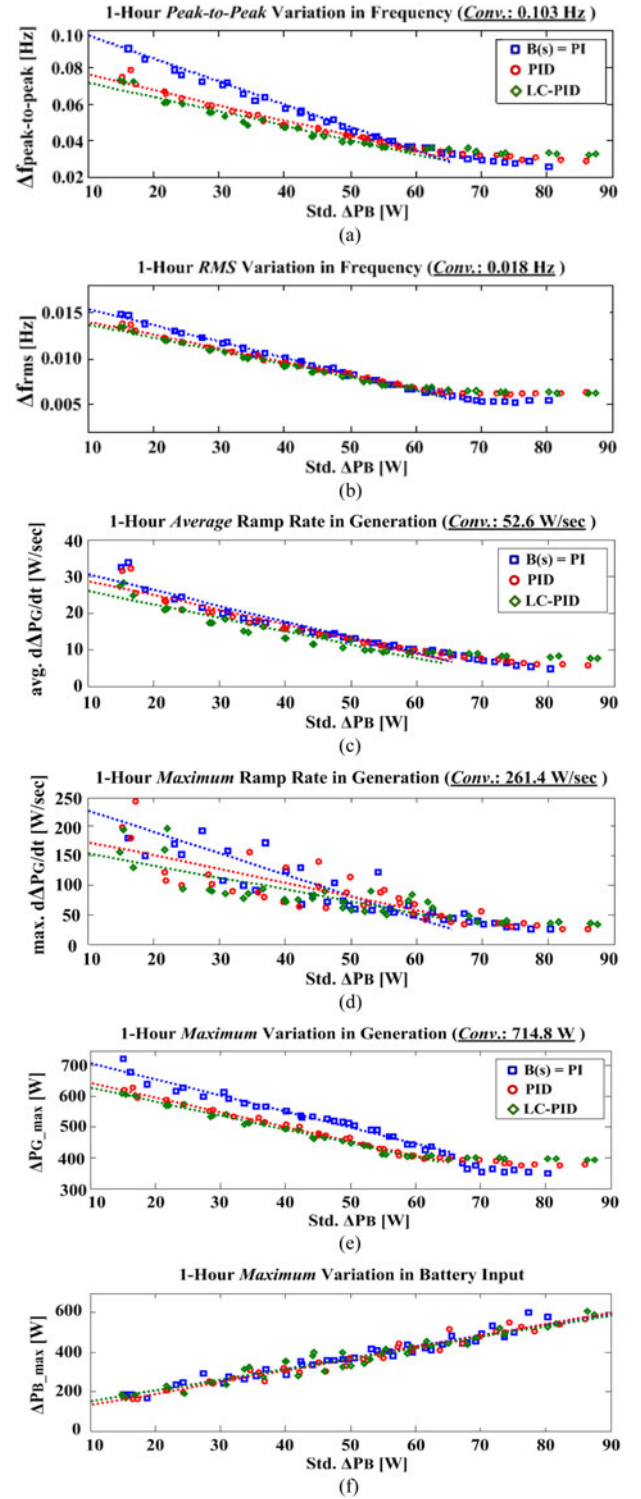
Fig. 25. (a) $\Delta f_{\mathrm{peak-to-peak}}$, (b) Δf_{rms}, (c) *avg.* $d\Delta P_{\mathrm{G}}/dt$, (d) max. $d\Delta P_{\mathrm{G}}/dt$, (e) $\Delta P_{G\_\mathrm{max}}$, and (f) $\Delta P_{B\_\mathrm{max}}$ in the test grid due to the proposed GFR.

increasing the magnitude and variation of $\Delta P_{B\_\mathrm{ref}}$. For the one-hour experiments, T_B in (7) was randomly varied between 0.1 s and 0.2 s every 10 minutes based on [42]. As described in Fig. 8(a), the use of different values can still ensure the effective contribution of the BESSs to the real-time GFR. It can be

Fig. 26. SOC variations, $\Delta\text{SOC} = \text{SOC}|_{t=0} - \text{SOC}|_{t=1\,h}$, of the Li-ion battery pack during the 1-hour case studies. Note $-1\% \le \Delta\text{SOC} \le 1\%$ in most experiments.
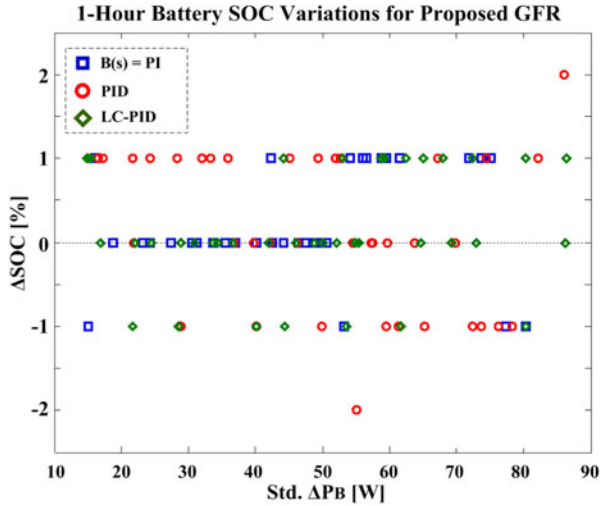
seen in Fig. 25 that the DLC-enabled behind-the-meter BESSs contributed to reducing the frequency deviations, as well as the ramp-rates and the maximum variations in the total output of DGs. The PID and LC-PID controllers led to smaller Δf, $d\Delta P_{\text{G}}/dt$, and ΔP_{G_max} for relatively small values of *std.* ΔP_B, which can also be explained using the Bode plots in Fig. 11.

The experimental studies demonstrated the simulation case studies discussed in Section IV. The simulation results obtained using the comprehensive model of the building-power-system, while considering random communication delays, were consistent with the experimental results obtained by controlling the inverter-interfaced battery pack according to (7). In other words, Figs. 19 and 25 consistently show that the proposed GFR method linearly decreased Δf, $d\Delta P_{\text{G}}/dt$, and ΔP_{G_max}, as *std.* ΔP_B was increased.

The proposed GFR scheme did not significantly affect the SOC levels of the behind-the-meter BESSs. In Fig. 26, the total variations in the SOC of the battery pack, corresponding to the 1-hour case studies, are in the range -1% to $+1\%$ for most values of *std.* ΔP_B, which implies that the life of the battery is not greatly affected. This is mainly because the battery compensated for the high-frequency components of the SFC signals. The simple first-order LPF could effectively remove the DC offset in the DLC signals. Since the battery modeled the total response of the building BESSs, Fig. 26 equivalently represents the total SOC variations of the BESSs considered in the simulation case studies.

VI. CONCLUSION

This paper proposes a new real-time GFR scheme in which behind-the-meter electrical BESSs compensate for rapid load demand variations through DLC. An electrical system of a commercial building, as well as coordination of the building- and device-level controllers, was developed to enable the building to act as a large-scale inverter-interfaced stationary BESS, par-
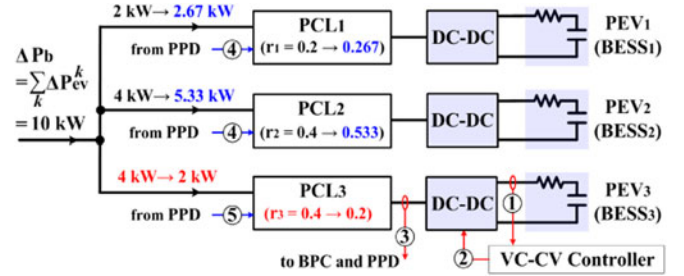
ticularly from the viewpoint of the ISO. Small-signal analysis was conducted using the dynamic responses of the aggregated generators and the behind-the- meter BESSs, considering three different types of $B(s)$. Simulation and experimental case studies were carried out using the comprehensive building model and its simplified transfer function model, respectively. The one-hour case study results consistently showed that the proposed GFR method effectively reduced Δf, $d\Delta P_{\text{G}}/dt$, and ΔP_{G_max}, as the penetration of DLC-enabled behind-the-meter BESSs increased.

APPENDIX

A. Distribution of DLC Signal to Behind-the-Meter BESSs via Coordination of Building-Level and Device-Level Controllers

In Fig. 1(b), the BPC determines $P_{\text{tot\_ev}}$ based on the DLC signal ΔP_{b_ref}, the PEV charging demand $\sum_k P_{\text{ev\_ss}}^k$, and the rooftop PV output P_{pv}. The BPC can simply adjust the input power variation of the BESSs $\sum_k \Delta P_{\text{ev}}^k$ to track ΔP_{b_ref}, for a building where the charging demand is constant in steady state and no rooftop PV generator exists. The DLC is overridden if none of the PEVs are available for the GFR ancillary service provision (i.e., $P_{\text{ev}}^k = P_{\text{ev\_max}}^k$ or $V_{\text{ev}}^k = V_{\text{ev\_max}}^k$ for all k). In particular, during the override period in which all the PEVs operate at maximum voltage levels, the BPC controls the duty ratio controller of the AC-DC converter to decrease $P_{\text{tot\_ev}}$ and thereby maintain the building energy balance.

The PPD controls the individual input power P_{ev}^k of the PEVs. In this study, the ratio r_k of the input power of the kth PEV to the total input power of the PEVs was initially determined as (8) based on S_{ev}^k and t_d^k; i.e., P_{ev}^k was initially set to $r_k \times P_{\text{tot\_ev}}$.

$$r_k = \frac{(1 - S_{\text{ev}}^k)/t_d^k}{\sum_k (1 - S_{\text{ev}}^k)/t_d^k}, \quad \text{for } k = 1, 2, \dots, K. \quad (8)$$

If the uth PEV is fully recharged or disconnected, the corresponding VC-CV controller decreases r_u and thereby P_{ev}^u, gradually to zero. The PPD then controls $r_{k\neq u}$ and $P_{\text{ev}}^{k\neq u}$ of the other PEVs to make ΔP_b track ΔP_{b_ref} continuously. As shown in Fig. 27, this is achieved using programmable current limiters (PCLs) [44]. The numbers indicate the order of the signal activations when the input power of PEV$_3$ decreases to prevent the battery overvoltage. The input power of PEV$_1$ and PEV$_2$ then increases proportional to r_1 and r_2 to make ΔP_b track ΔP_{b_ref}.

Fig. 27. Coordination of the BPC, PPD, and VC-CV controller to make ΔP_b track ΔP_{b_ref} by controlling the total input power variation of BESSs $\sum_k \Delta P_{\text{ev}}^k$.

TABLE V
OPERATIONS OF THE BPC AND PPD FOR DLC SIGNAL DISTRIBUTION

Controllers	PEV Conditions	Operation Sets
BPC	$L > 0$	$P_b = P_{b\_ref}$ (i.e., $\Delta P_b = \Delta P_{b\_ref}$)
	$L = 0$	If $P_{sur} = 0$, then maintain P_b at P_{b_ref}
		Otherwise, increase or decrease P_b.
PPD	$L = K$	Maintain all r_h as constant
	$0 < L < K$	Decrease r_g and increase r_h as proportional to the values of r_h
	$L = 0$	Maintain all r_g at zero

Table V lists the complete set of operations of the BPC and the PPD, where L is the number of PEVs capable of responding to the DLC signals. In addition, h and g are the indices of the PEVs L and (K-L), respectively. The surplus power inside the building P_{sur} is given by

$$P_{sur} = P_b + P_{pv} - \sum_k P_{ev}^k - P_{load}. \quad (9)$$

B. ZIP model for DC Loads in the DLC-Enabled Building

The polynomial expression (10) in [45] was used to model the DC loads connected to the DC-link. Note that the DLC-enabled building still includes AC loads, as shown in Fig. 1. The load profile was adopted from [46] and scaled up such that the maximum building load was equal to 530 kW. The DC load was assumed to take 20% of the total building load.

$$P_{load} = P_{load\_ref} \left[0.76 \left(\frac{V_{load}}{208} - 0.52 \frac{V_{load}}{208} + 0.76 \right) \right]. \quad (10)$$

REFERENCES

[1] M. A. Hanley, "Frequency instability problems in North American Interconnections," Nat. Energy Technol. Lab. (DOE/ NETL-2011/1473), May 1, 2011. [Online]. Available: http://www.netl.doe.gov/energy-analyses/temp/FY11_FrequencyInstabilityProblemsinNorthAmerican Interconnections_060111.pdf
[2] J. Neubauer and M. Simpson, "Deployment of behind-the-meter energy storage for demand charge reduction," Nat. Renewable Energy Lab. (NREL/TP-5400-63162), Jan. 2015. [Online]. Available: http://www.nrel.gov/docs/fy15osti/63162.pdf
[3] Stem Inc., [Online]. Available: https://www.technologyreview.com/s/506776/a-startups-smart-batteries-reduce-buildings-electric-bills/
[4] N. S. Pearre, W. Kempton, R. L. Guensler, and V. V. Elango, "Electric vehicles: how much range is required for a day's driving?," *Transport. Res. Part C*, vol. 19, no. 6, pp. 1171–1184, Dec. 2011.
[5] T. Masuta and A. Yokoyama, "Supplementary load frequency control by use of a number of both electric vehicles and heat pump water heaters," *IEEE Trans. Smart Grid*, vol. 3, no. 3, pp. 1253–1262, Sep. 2012.
[6] T. Markel *et al.*, "PHEV energy storage performance/life/cost trade-off analysis," in *Proc. Adv. Automotive Battery Conf.*, Tampa, FL, USA, May 2008.
[7] P. M. R *et al.*, "Electric vehicles participating in frequency control: Operating islanded systems with large penetration of renewable power sources," in *Proc. IEEE PowerTech Conf.*, Trondheim, Norway, Jun. 2011, pp. 1–6.
[8] J. R. Pillai and B. Bak-Jensen, "Vehicle-to-grid for islanded power system operation in Bornholm," in *Proc. IEEE Power & Energy Soc. General Meeting*, Minneapolis, MN, USA, Jul. 2010, pp. 1–8.
[9] S. Izadkhast, P. Garcia-Gonzalez, and P. Frías, "An aggregate model of plug-in electric vehicles for primary frequency control," *IEEE Trans. Power Syst.*, vol. 30, no. 3, pp. 1475–1482, May 2015.

[10] Y. Mu, J. Wu, J. Ekanayake, N. Jenkins, and H. Jia, "Primary frequency response from electric vehicles in the Great Britain power system," *IEEE Trans. Smart Grid*, vol. 4, no. 2, pp. 1142–1150, Jun. 2013.
[11] H. Liu, Z. Hu, Y. Song, and J. Lin, "Decentralized vehicle-to-grid control for primary frequency regulation considering charging demands," *IEEE Trans. Power Syst.*, vol. 28, no. 3, pp. 3480–3489, Aug. 2013.
[12] H. Liu, Z. Hu, Y. Song, J. Wang, and X. Xie, "Vehicle-to-grid for supplementary frequency regulation considering charging demands," *IEEE Trans. Power Syst.*, to be published.
[13] Y. Ota *et al.*, "Autonomous distributed V2G (vehicle-to-grid) satisfying scheduled charging," *IEEE Trans. Smart Grid*, vol. 3, no. 1, pp. 559–564, Mar. 2012.
[14] Q. R. Hamid and J. A. Barria, "Distributed recharging rate control for energy demand management of electric vehicles," *IEEE Trans. Power Syst.*, vol. 28, no. 3, pp. 2688–2699, Aug. 2013.
[15] M. Datta and T. Senjyu, "Fuzzy control of distributed PV inverters/energy storage systems/electric vehicles for frequency regulation in a large power system," *IEEE Trans. Smart Grid*, vol. 4, no. 1, pp. 479–488, Mar. 2013.
[16] H. Yang *et al.*, "Application of plug-in electric vehicles to frequency regulation based on distributed signal acquisition via limited communication," *IEEE Trans. Power Syst.*, vol. 28, no. 2, pp. 1017–1026, May 2013.
[17] M. D. Galus, S. Koch, and G. Andersson, "Provision of load frequency control by PHEVs, controllable loads, and a cogeneration unit," *IEEE Trans. Ind. Electron.*, vol. 58, no. 10, pp. 4568–4582, Oct. 2011.
[18] O. Leitermann, "Energy storage for frequency regulation on the electric grid," Ph.D. dissertation, Dept. Elect. Eng. Commun. Sci., Massachusetts Inst. Technol., Cambridge, MA, USA, Jun. 2012, Ch. 2 and 6.
[19] Kempton and J. Tomic, "Vehicle-to-grid power implementation: From stabilizing the grid to supporting large-scale renewable energy," *J. Power Sources*, vol. 144, no. 1, pp. 280–294, Jun. 2005.
[20] Y. Lin, P. Barooah, S. Meyn, and T. Middelkoop, "Experimental evaluation of frequency regulation from commercial building HVAC systems," *IEEE Trans. Smart Grid*, vol. 6, no. 2, pp. 776–783, Feb. 2015.
[21] H. Hao *et al.*, "Aggregate flexibility of thermostatically controlled loads," *IEEE Trans. Power Syst.*, vol. 30, no. 1, pp. 189–198, Jan. 2015.
[22] R. Ma *et al.*, "Smart grid communication: its challenges and opportunities," *IEEE Trans. Smart Grid*, vol. 4, no. 1, pp. 36–46, Mar. 2013.
[23] Y. Kim, L. K. Norford, and J. L. Kirtley Jr., "Analysis of a building power system with a rooftop PV array and PHEVs as an aggregator," in *Proc. IEEE Innovative Smart Grid Tech. Conf.*, Washington, DC, USA, Feb. 2013, pp. 1–6.
[24] Society of Automotive Engineering (SAE), Electric Vehicle and Plug-in Hybrid Electric Vehicle Conductive Charge Coupler (J1772), Jan. 2010.
[25] L. Dickerman and J. Harrison, "A new car, a new grid," *IEEE Power Energy Mag.*, vol. 8, no. 2, pp. 56–61, Apr. 2010.
[26] O. Tremblay, L. A. Dessaint, and A. I. Dekkiche, "A generic battery model for the dynamic simulation of hybrid electric vehicles," in *Proc. Vehicle Power Propulsion Conf.*, Arlington, TX, USA, Sep. 2008, pp. 1–6.
[27] M. Chen and G. A. Rincon-Mora, "Accurate electrical battery model capable of predicting runtime and I-V performance," *IEEE Trans. Energy Convers.*, vol. 21, no. 2, pp. 504–511, Jun. 2006.
[28] Y. Kim, L. K. Norford, and J. L. Kirtley, "Modeling and analysis of a variable speed heat pump for frequency regulation through direct load control," *IEEE Trans. Power Syst.*, vol. 30, no. 1, pp. 397–408, Jan. 2015.
[29] P. Kunder, *Power System Stability and Control*. Toronto, ON, Canada: McGraw-Hill, 1994, pp. 581–626.
[30] X. Yu and K. Tomsovic, "Application of linear matrix inequalities for load frequency control with communication delays," *IEEE Trans. Power Syst.*, vol. 19, no. 3, pp. 1508–1515, Aug. 2004.
[31] L. Jiang, W. Yao, Q. H. Wu, J. Y. Wen, and S. J. Cheng, "Delay dependent stability for load frequency control with constant and time-varying delays," *IEEE Trans. Power Syst.*, vol. 27, no. 2, pp. 932–941, May 2012.
[32] A. D. Papalexopoulos and P. E. Andrianesis, "Performance-based pricing of frequency regulation in electricity markets," *IEEE Trans. Power Syst.*, vol. 29, no. 1, pp. 441–449, Jan. 2014.
[33] H. Hao, B. M. Sanandaji, K. Poolla, and T. L. Vincent, "Frequency regulation from flexible loads: Potential, economics, and implementation" in *Proc. Amer Control Conf.*, Portland, OR, USA, Jun. 2014, pp. 65–72.
[34] Federal Energy Regulatory Commission, "Frequency Regulation Compensation in the Organized Wholesale Power Markets," Oct. 2011.
[35] Y. V. Makarov, L. S. J. Ma, and T. B. Nguyen, "Assessing the value of regulation resources based on their time response characteristics," Pacific Northwest Nat. Lab. (Tech. Rep. PNNL-17632), Jun. 2008. [Online]. Available: http://www.pnl.gov/main/publications/external/technical_reports/PNNL-17632.pdf

[36] Univ. Michigan, "Control tutorials for matlab & simulink: extras: designing lead and lag compensators." [Online]. Available: http://ctms.engin.umich.edu/CTMS/index.php?aux = Extras_Leadlag

[37] B. Zhang and J. Baillieul, "A two level feedback system design to provide regulation reserve," in *Proc. IEEE Conf. Decision Control*, Dec. 10–13, 2013, pp. 4322–4328.

[38] D. J. Lee and L. Wang, "Small signal stability analysis of an autonomous hybrid renewable energy power generation/energy storage system part I: Time-domain simulations," *IEEE Trans. Energy Convers.*, vol. 23, no. 1, pp. 311–320, Mar. 2008.

[39] W. H. Kersting, IEEE "Radial distribution test feeders," *IEEE Trans. Power Syst.*, vol. 6, no. 3, pp. 975–985, Aug. 1991.

[40] Fast Response Regulation Signal. [Online]. Available: http://www.pjm.com/markets-and-operations/ancillary-services/

[41] E. Ela, V. Gevorgian, A. Tuohy, B. Kirby, M. Milligan, and M. O'Malley, "Market designs for the primary frequency response ancillary service—Part I: motivation and design," *IEEE Trans. Power Syst.*, vol. 29, no. 1, pp. 421–431, Jan. 2014.

[42] T. Senjyu, T. Nakaji, K. Uezato, and T. Funabashi, "A hybrid power system using alternative energy facilities in isolated island," *IEEE Trans. Energy Convers.*, vol. 20, no. 2, pp. 406–414, Jun. 2005.

[43] Y. Wang, G. Delille, H. Bayem, X. Guillaud, and B. Francois, "High wind power penetration in isolated power systems—assessment of wind inertial and primary frequency responses," *IEEE Trans. Power Syst.*, vol. 28, no. 3, pp. 2412–2420, Aug. 2013.

[44] Linear Technology LTC4000 High Voltage High Current Controller for Battery Charging and Power Management. [Online]. Available: http://www.linear.com/docs/39757, Linear Technology

[45] A. Bokhari *et al.*, "Experimental determination of the ZIP coefficients for modern residential, commercial, and industrial loads," *IEEE Trans. Power Del.*, vol. 29, no. 3, pp. 1372–1381, Jun. 2014.

[46] D. H. Blum, "Analysis and characterization of ancillary service demand response strategies for variable air volume HVAC systems," M.S. thesis, Dept. Arch., Massachusetts Inst. Technol., Cambridge, MA, USA, Jun. 2013.

Young-Jin Kim (S'14-M'15) received the B.S. and M.S. degrees in electrical engineering from Seoul National University, in 2007 and 2010, respectively, and the Ph.D. degree in electrical engineering from Massachusetts Institute of Technology, Cambridge, MA, USA. He worked for Korea Electric Power Corporation as a Power Transmission and Distribution System Engineer from 2007 to 2011. He was also a Visiting Scholar at the Catalonia Institute for Energy Research in 2014, and a Postdoctoral Researcher for the Center for Energy, Environmental, and Economic Systems Analysis, Energy Systems Division, Argonne National Laboratory, from 2015 to 2016.

He joined the Faculty of the Pohang University of Science and Technology (POSTECH) in 2016, where he is currently an Assistant Professor in the Department of Electrical Engineering. His research fields of interests include distributed generators, renewable energy resources, and smart buildings.

Gerard Del-Rosario-Calaf received the M.S. degree in engineering from the School of Engineering of Barcelona (ETSEIB), Technical University of Catalonia Barcelona (UPC), in 2008.

He currently works as a Project Engineer at the Smart Grids and Energy Economics Group of the Catalonia Institute for Energy Research (IREC) . His research interests include modeling and simulation of power systems for distribution network management studies and the development of experimental setups regarding demand response mechanisms.

Leslie K. Norford received the B.S. degree in engineering science from Cornell University, Ithaca, NY, USA, in 1973 and the Ph.D. degree in mechanical and aerospace engineering from Princeton University, Princeton, NJ, USA, in 1984.

He is currently Professor of Building Technology in the Department of Architecture, Massachusetts Institute of Technology. His research interests include monitoring the performance of mechanical and electrical equipment in buildings, optimization techniques as applied to the design and operation of buildings and their mechanical systems, and measurements and simulations of the interaction of buildings with electricity distribution systems and urban environments.